

Double side passivation of phenylethyl ammonium iodide for all perovskite tandem solar cell with efficiency of 26.8%

Huan Bi^{1,2}  | Jiaqi Liu¹  | Liang Wang¹  | Zheng Zhang¹  |
 Gaurav Kapil¹  | Shahrir Razey Sahamir¹  | Ajay Kumar Baranwal¹  |
 Yuyao Wei²  | Yongge Yang² | Dandan Wang² | Takeshi Kitamura^{1,2}  |
 Hiroshi Segawa³  | Qing Shen^{1,2}  | Shuzi Hayase^{1,2} 

¹i-Powered Energy System Research Center (i-PERC), The University of Electro-Communications, Tokyo, Japan

²Faculty of Informatics and Engineering, The University of Electro-Communications, Tokyo, Japan

³Research Center for Advanced Science and Technology, The University of Tokyo, Tokyo, Japan

Correspondence

Hiroshi Segawa, Huan Bi, Qing Shen and Shuzi Hayase.

Email: csegawa@mail.ecc.u-tokyo.ac.jp, hbi.trans.sci@mail.uec.jp, shen@pc.uec.ac.jp and hayase@uec.ac.jp

Funding information

NEDO; the New Energy and Industrial Technology Development, Grant/Award Number: JPNP20015

Abstract

All-perovskite tandem solar cells are regarded as the next generation of devices capable of enhancing the solar energy utilization rate. Unlike single-junction perovskite solar cells (PSCs), the efficacy of tandem cells is contingent upon the performance of both the top and bottom cells. In this study, we employed a simultaneous co-modification strategy to incorporate phenylethylammonium iodide (PEAI) at both the top and bottom interfaces of the perovskite film, aiming to boost the top cell's performance. Both experimental and theoretical findings indicate that PEAI not only elevates the perovskite film quality through chemical interactions but also mitigates nonradiative recombination within the device. Consequently, the efficiency of the wide-bandgap (1.77 eV) PSCs based on nickel oxide (NiO_x) attained a level of 16.5%. Simultaneously, the all-perovskite tandem solar cells achieved an efficiency of 26.81% and demonstrated superior stability.

KEY WORDS

all perovskite tandem solar cells, co-modification, nonradiative recombination, PEAI, perovskite solar cells

1 | INTRODUCTION

Over the last decade, organic-inorganic hybrid perovskite materials have gained prominence in applications such as solar cells, light-emitting diodes, and memory devices, attributed to their superior light absorption properties, extended carrier diffusion lengths, and robust defect tolerance etc.^{1,2} Among various developments, single-junction perovskite solar cells (PSCs) have

achieved a certified power conversion efficiency (PCE) exceeding 26%.³ Moreover, all-perovskite tandem solar cells, designed to enhance solar energy conversion efficiency, have garnered significant interest.^{4–6} These tandem cells typically combine wide and narrow bandgap PSCs. While recent advancements have seen narrow bandgap PSCs reaching a PCE of 23.6%, wide bandgap PSCs lag behind in achieving comparable efficiency levels.⁷ Thus, optimizing the performance of wide

This is an open access article under the terms of the [Creative Commons Attribution](#) License, which permits use, distribution and reproduction in any medium, provided the original work is properly cited.

© 2024 The Author(s). *EcoEnergy* published by John Wiley & Sons Australia, Ltd on behalf of China Chemical Safety Association.

bandgap PSCs is crucial for harmonizing the efficiencies of both solar cell types.

Nickel oxide (NiO_x), serving as an inorganic hole transport layer (HTL), is extensively utilized in PSCs owing to its superior stability, high transparency, and compatible energy levels.^{8–10} However, significant non-radiative recombination is observed at the NiO_x /perovskite interface, prompting numerous studies aimed at enhancing this interface. Many works have been reported to improve the NiO_x /perovskite (PVK) interface.^{11–14} He et al. implemented a molecular modification approach to fabricate NiO_x -based inverted PSCs with F6TCNNQ modification. This modification substantially reduced the energy offset between the NiO_x and perovskite layers from 0.18 to 0.04 eV, facilitating more efficient hole extraction from the perovskite film to the NiO_x HTL. Consequently, the device incorporating F6TCNNQ achieved a remarkable PCE of 20.86%.¹¹ Similarly, Zhang et al. introduced a bottom interface modification strategy, ultimately achieving PSCs with an efficiency of 21.62% by incorporating polyethylene oxide.¹² Thus, enhancing the NiO_x /perovskite interface contact is crucial for further improving device efficiency.

Furthermore, the PVK/ C_{60} interface exhibits a significant amount of non-radiative recombination, which adversely impacts the performance of the device. This behavior is primarily attributed to the fact that the energy levels presented in the perovskite and fullerene sides are misaligned. Specifically, when there are mismatches between the conduction band of PVK and the LUMO level of C_{60} , the charge carriers are trapped at these energy levels. The trapped electrons recombine non-radiatively rather than participate in the generation of electric current, leading to the decline in efficiency.¹⁵ Additionally, the non-radiative recombination is indeed facilitated by the presence of interface disorders. For instance, newly formed dislocations and impurities create trap states that help in the recombination process. Compounded by the fact that many perovskites and C_{60} are morphologically incompatible hence making the contact poor with incomplete surface coverage at the top, the non-radiative recombination is increased.¹⁶ Consequently, the various approaches designed to improve the perovskite top interface have been designed.¹⁷ These include improving the deposition techniques to produce smoother and more continuous C_{60} layer that reduces the number of the defects and improves energy level alignments. Such approaches seek to reduce the level of the interface traps as well as a morphological compatibility between the PVK and C_{60} layers thus mitigates some of the non-radiative recombination hence improve the device.¹⁶ Zhang et al. introduced a post-treatment method using tetra-n-octadecyl ammonium bromide (TODB), which diverges

from prior approaches by utilizing long-chain molecules for the modification of the perovskite top interface. This method involves large cations adhering to the perovskite surface for modification, TODB selectively passivating defects at the interface owing to its ionic nature, and the anticipation that ultralong alkyl chains will further refine the interfacial properties of the perovskite films. As a result, devices treated with TODB have achieved efficiencies exceeding 20% alongside remarkable stability.¹⁸ Our previous research has also underscored the significance of top interface modification in enhancing the quality of perovskite films and reducing nonradiative recombination in devices.^{19–21} By deploying suitable materials for top interface modification, we have notably advanced the performance and durability of the devices.

As we all know, due to the particularity of perovskite materials, the properties, and defects of perovskite films with different element ratios and different band gaps are completely different. This is why many modified materials that have been proven to be effective, when replacing the perovskite composition, showed completely different results. On the other hand, collaborative modification is also a big challenge. There are few works reporting collaborative strategies to improve device performance. This is mainly due to the fact that when trying to change the substrate for perovskite film deposition, the quality, defects, and energy bands of the film will all change. Therefore, we advocate for a comprehensive double-sided passivation approach by applying phenylethyl ammonium iodide (PEAI) at both the top and bottom wide-bandgap perovskite interfaces. Through both theoretical analysis and experimental validation, we have demonstrated the intricate chemical interactions between PEAI, the perovskite material, and NiO_x . These interactions significantly enhance the perovskite film's quality, leading to a reduction in bulk nonradiative recombination and stronger interface cohesion. Moreover, the diminution of interface defects contributes to a decrease in non-radiative recombination at the interfaces. Consequently, our approach facilitated single-junction wide-bandgap PSCs to achieve a notable PCE of 16.5%, alongside an enhancement in device stability. Additionally, the PEAI-modified all-perovskite tandem solar cell achieved an outstanding champion PCE of 26.81%.

2 | RESULTS AND DISCUSSION

In this study, the configuration of the top cell utilized was ITO/ NiO_x /(PEAI)/PVK (FA_{0.8}Cs_{0.2}PbI_{1.8}Br_{1.2})/(PEAI)/ C_{60} /BCP/Ag, with the fabrication process illustrated in Figure 1A. PEAI was introduced concurrently at the top and bottom interfaces of the device. X-ray photoelectron

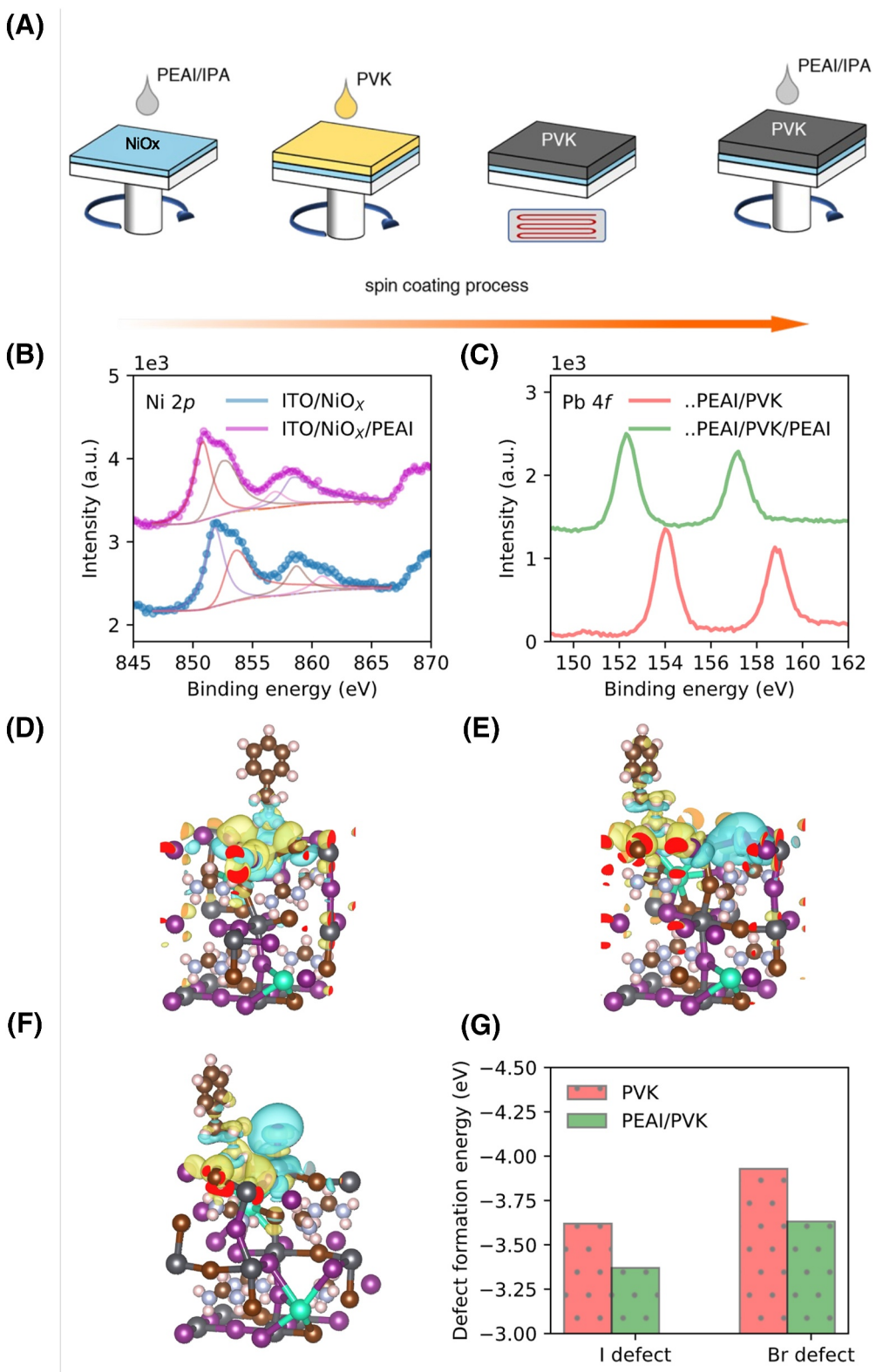


FIGURE 1 (A) Schematic diagram of PEAI co-modification strategy. XPS spectra of the PEAI with (B) NiO_x Ni 2p and (C) perovskite Pb 4f. The surfaces for the perovskite with the (D) I-defect, (E) Br-defect, and (F) perfect surface contact with the PEAI. (G) Defect (I-defect and Br-defect) formation energy of the perovskite film with or without PEAI modification.

spectroscopy (XPS) measurements confirmed the presence of PEAI on the NiO_x surface. Notably, the I 3d signal was absent on the bare ITO/ NiO_x interface but was distinctly observed on the ITO/ NiO_x /PEAI interface, indicating successful adsorption of PEAI on the NiO_x film (Figure S1a). Furthermore, XPS analyses revealed shifts in the Ni 2p and O 1s signals upon PEAI application, as shown in Figure 1B and Figure S1b, suggesting a robust chemical interaction between NiO_x and PEAI that ensures the stable adsorption of PEAI on the NiO_x film, resistant to displacement by subsequent perovskite solutions. Additional XPS evidence of chemical interactions between PEAI and the perovskite film was observed, as presented in Figure 1C, with Pb 4f and I 3d signals shifting toward lower binding energies post-PEAI modification (Figure S1c). Next, we used Fourier Transform Infrared Spectroscopy to further reveal the chemical interaction between NiO_x and PEAI.²² As shown in the Figure S2, we tested the infrared signals of PEAI powder, ITO/ NiO_x and ITO/ NiO_x /PEAI respectively. The results show that compared with ITO/ NiO_x , ITO/ NiO_x /PEAI has many characteristic peaks of PEAI, which shows that PEAI does exist on the NiO_x film (it should be noted that in the preparation procedure of ITO/ NiO_x /PEAI, we finally used The DMF/DMSO mixed solvent rinsed the surface and further annealed it), even after the mixed solvent rinse. Then we compared the infrared signals of ITO/ NiO_x /PEAI and PEAI powders and partially amplified them. As shown in the figure, 690 and 740 cm^{-1} are usually attributed to the C-H bending vibration of aromatic rings, especially in benzene ring structures. The vibration at 940 cm^{-1} usually corresponds to the C-H bending vibration, especially in benzene rings or other types of cyclic hydrocarbons. The vibration at 1250 cm^{-1} usually corresponds to some type of C-N stretching vibration.²³ This vibrational signature is due to the vibration of the chemical bond between carbon and nitrogen. The infrared results show that there is a strong chemical interaction between PEAI and NiO_x , which is consistent with the XPS results. In addition, we believe that it is precisely because of these effects that the signal of PEAI can still be detected even if the NiO_x /PEAI surface is rinsed with mixed solvents. These interactions are anticipated to enhance the perovskite film's quality and the device's overall performance.

The interaction between PEAI and perovskite was further substantiated through density functional theory (DFT) calculations. We investigated three distinct perovskite surfaces: iodine-deficient (initial model S3a and optimized model S3d), bromine-deficient (initial model S3b and optimized model S3e), and defect-free (initial model S3c and optimized model S3f). As shown in Figure 1D–F, charge transfer analysis was utilized to

assess the interaction between PEAI and perovskite across these surfaces, revealing significant charge migration upon contact with PEAI. This indicates a robust chemical interaction, anticipated to not only passivate existing surface defects (iodine or bromine deficiencies) but also enhance interface adhesion. It should be noted that since DFT cannot distinguish between the upper and lower interfaces, the results of DFT can not only show that PEAI can effectively improve the interface contact of the lower interface, but also improve the film quality and interface contact of the upper interface. In addition, the introduction of PEAI will also increase the defect formation energy of the perovskite film. As shown in Figure 1G, when perovskite is deposited on the PEAI substrate, both I defects and Br defects show higher defect formation energy. This means that more energy is required to form these defects, and therefore, defects during film formation can be effectively reduced. Unlike mere defect passivation, completely blocking defect formation (during film formation) can significantly improve film quality (especially bulk quality). In summary, both empirical and theoretical evidence confirms a significant chemical interaction between PEAI and perovskite, and underscoring its potential to enhance perovskite film quality.

The chemical interaction between PEAI and the perovskite film motivated us to further investigate its impact on film quality. UV-Vis absorption measurements indicate a slight increase in the intensity for devices incorporating PEAI both between the ITO/ NiO_x interfaces and atop the perovskite film, compared to the baseline ITO/ NiO_x /PVK configuration (refer to Figure S4a), the perovskite film thickness tests (Figure S4b) show an increase in the thickness of perovskite films deposited on PEAI substrates, which is consistent with previous reports that changing the film's deposition substrate changes the thickness of the film.²⁴ The band gap values of these films consistently register at 1.77 eV. Moreover, Urbach energy analysis, detailed in Figure S5, corroborates the positive effect of PEAI on film quality: a reduction in Urbach energy from 59.00 meV in the control sample to 38.88 meV in films modified by PEAI at both interfaces.²⁵ This result prove that the perovskite film became more ordered, which means fewer defects in the perovskite film after co-PEAI modified. Scanning electron microscopy (SEM) observations suggest a marginal increase in grain size following PEAI treatment, particularly notable in films with bottom interface modifications (Figure 2A–C), attributing this change to alterations in the film's growth substrate and consequent adjustments in the growth process, aligning with prior studies.²⁴ X-ray diffraction (XRD) (Figure S6) analysis further supports these findings, showing

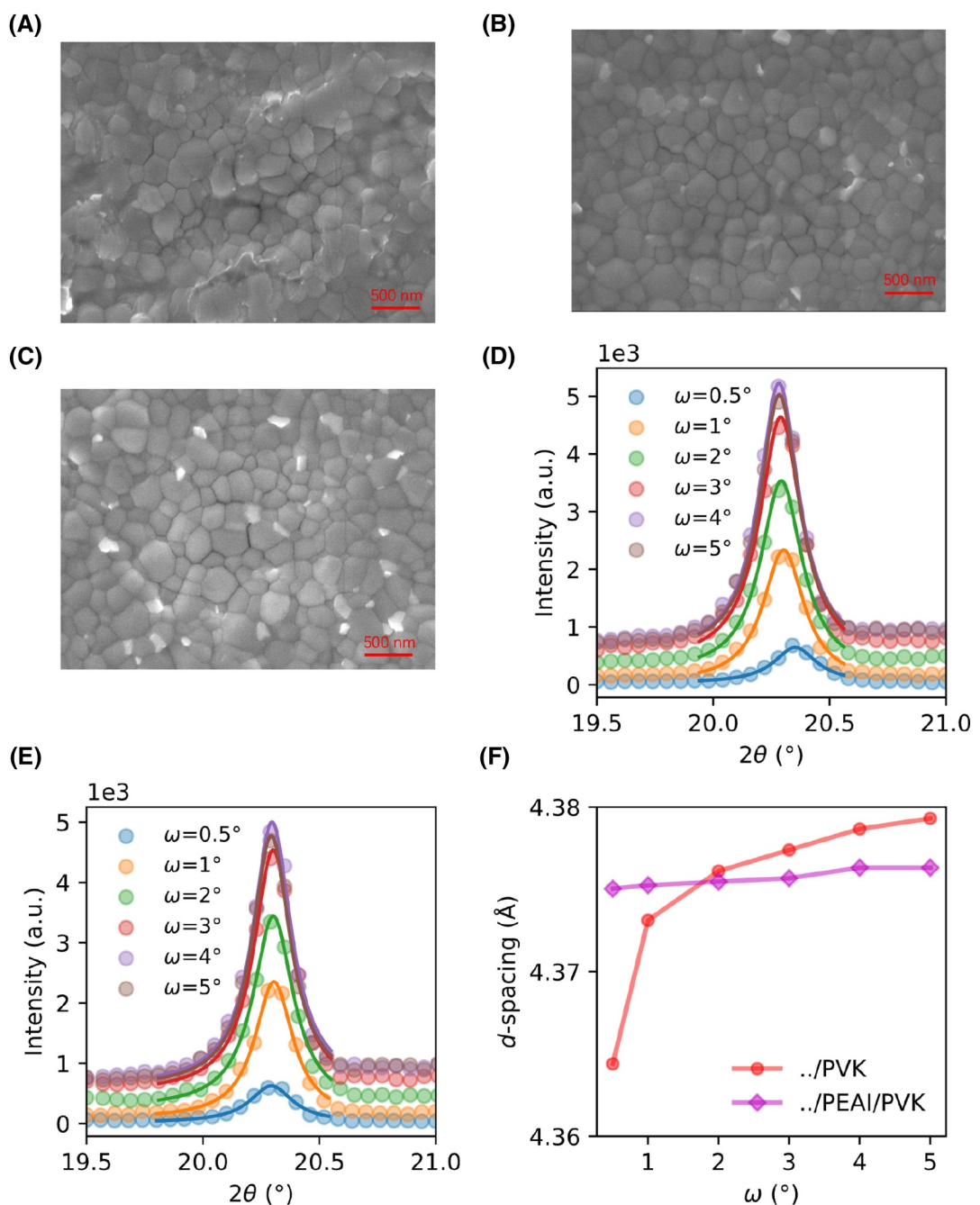


FIGURE 2 SEM image of the film with the structure of (A) ITO/NiO_x/PVK, (B) ITO/NiO_x/PEAI/PVK, and (C) ITO/NiO_x/PEAI/PVK/PEAI. GIXRD patterns of the perovskite films based on (D) ITO/NiO_x/PVK and (E) ITO/NiO_x/PEAI/PVK. (F) d -spacing values obtained from (D, E) as a function of incidence angle.

enhanced peak intensities post-PEAI integration, indicative of improved crystallinity in the perovskite film. To elucidate the mechanism behind the enhanced quality of perovskite films through bottom modification, we evaluated the water contact angle, with findings presented in Figure S7. We tested the water contact angle of different device structures (ITO/NiO_x (control) and ITO/NiO_x/PEAI (target)). As a result, because NiO_x has super hydrophilicity, the contact angle is very small and has

exceeded the possible test range of the instrument. However, we found that compared to the control device, the target device showed a larger hysteresis, which means that water spreads more easily on the NiO_x/PEAI surface, which also reflects that PEAI can further reduce the water contact of NiO_x. This also leads to the subsequent formation of higher quality perovskite films.^{26,27} Additionally, Atomic Force Microscopy analysis revealed a decrease in surface roughness upon PEAI deposition on

NiO_x (see Figure S8), indicating that substrate modifications indeed can influence film quality.²⁴

Changes in the substrate have been reported also can affect the stress distribution in the perovskite film.²⁴ So, we further investigated the impact of PEAI on perovskite film stress by conducting depth-dependent Grazing Incidence X-ray Diffraction (GIXRD) analyses. For the ITO/ NiO_x /PVK structure, characteristic peak shifts toward lower angles were observed as incident angles (ω) increased from 0.5° to 5° , suggesting stress and strain in the film (illustrated in Figure 2D). Conversely, for the PEAI-modified interface (ITO/ NiO_x /PEAI/PVK), the peaks remained virtually unchanged over the same ω range, indicating a significant reduction in interfacial stress (shown in Figure 2E and 2F). Photoluminescence (PL) measurements provided additional insights into the modification's effectiveness, demonstrating a marked increase in PL intensity for the modified perovskite film compared to the control film. The intensity progression from glass/PVK to glass/PEAI/PVK, and further to glass/PEAI/PVK/PEAI, substantiates the role of PEAI in mitigating perovskite film defects (refer to Figure S9).

The enhanced film quality and significant chemical interactions prompted an investigation into the influence of PEAI on device performance. Figure 3A illustrates the characteristic current-voltage (*J-V*) curves for devices,

comparing those with and without PEAI modification (control: ITO/ NiO_x /PVK/C₆₀/BCP/Ag; bottom: ITO/ NiO_x /PEAI/PVK/C₆₀/BCP/Ag; both: ITO/ NiO_x /PEAI/PVK/PEAI/C₆₀/BCP/Ag). The photovoltaic parameters associated with these configurations are summarized in Table 1. The control device achieved a PCE of 10.72%, whereas devices modified at the bottom and both modifications exhibited PCEs of 15.46% and 16.37%, respectively. The external quantum efficiency (EQE) analysis corroborated the integrated current density values derived from the *J-V* curves, as shown in Figure 3B. Device stability, with and without PEAI modification, was assessed and documented in Figure 3C,D. Long-term

TABLE 1 Photovoltaic parameters of the champion control, bottom and both-modification devices measured under simulated AM 1.5 G one sun illumination of 100 mW cm^{-2} .

Device	J_{SC} [mA cm^{-2}]	V_{OC} [V]	FF [%]	PCE [%]
Control ^a	16.12	1.085	61.3	10.72
Bottom ^b	17.22	1.165	77.1	15.46
Both ^c	17.35	1.192	79.2	16.37

^aITO/ NiO_x /PVK/C₆₀/BCP/Ag.

^bITO/ NiO_x /PEAI/PVK/C₆₀/BCP/Ag.

^cITO/ NiO_x /PEAI/PVK/PEAI/C₆₀/BCP/Ag.

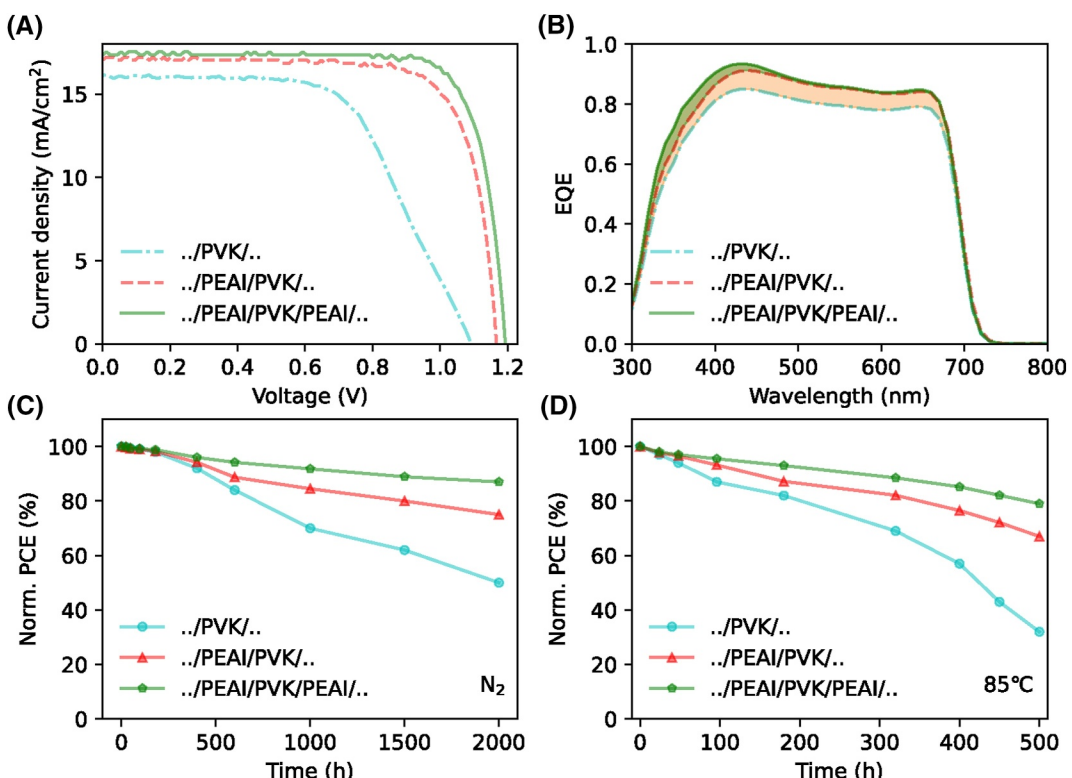


FIGURE 3 (A) *J-V* curves and (B) EQE spectra of the device with or without PEAI modification. (C) N_2 and (D) thermal stability of unpackaged devices which are stored in an N_2 -filled glove box.

stability tests of unencapsulated control and modified devices under a N₂ atmosphere revealed that after 2000 h, the control device retained 50% of its initial PCE, while the PEAI/PVK-based device maintained 75%, and the dual-modified device preserved 87% of their original PCEs (Figure 3C) after aging 2000 h. Thermal stability tests conducted at 85°C in darkness within a N₂ atmosphere, depicted in Figure 3D, demonstrated that the modified device sustained at least 79% of its initial PCE after 500 h, in contrast to the control device, which maintained only 32%. Literature suggests that device failure is exacerbated not solely by defect abundance but also by internal film stress leading to cracking and accelerated device degradation.²⁸ This work proved that the PEAI has been found to not only diminish film defects but also alleviate internal stresses, thereby enhancing device stability.

Such a significant increase in efficiency, we believe, is not just due to improvements in film quality, a systematic understanding of the underlying loss mechanisms is necessary. In the following, we apply the methodology introduced by Guillemoles et al. and Krückemeier et al. and quantitatively characterized the key loss mechanisms in our control and optimized PSCs by comparing the photovoltaic parameters short-circuit current density (J_{SC}), open-circuit voltage (V_{OC}), fill factor (FF) and PCE to the corresponding values estimated by the detailed balance (DB) model.^{29,30} The corresponding DB limit efficiency (PCE^{DB}) for a solar cell with a bandgap of 1.77 eV is estimated to be 27.74% with an ideal J_{SC} (J_{SC}^{DB}), ideal V_{OC} (V_{OC}^{DB}), and ideal FF (FF^{DB}) of 20.47 mA cm⁻², 1.483 V, and 91.33%, respectively.^{31,32} As a consequence, the normalized efficiency of a solar cell can be expressed as:²⁹

$$\frac{\text{PCE}}{\text{PCE}^{\text{DB}}} = \frac{J_{SC}}{J_{SC}^{\text{DB}}} \frac{V_{OC}}{V_{OC}^{\text{DB}}} \frac{\text{FF}}{\text{FF}^{\text{DB}}} \\ = \frac{J_{SC}}{J_{SC}^{\text{DB}}} \frac{V_{OC}^{\text{rad}}}{V_{OC}^{\text{DB}}} \frac{V_{OC}}{V_{OC}^{\text{rad}}} \frac{\text{FF}_0(V_{OC})}{\text{FF}^{\text{DB}}} \text{F}_{\text{FF}}^{\text{res}} \quad (1)$$

In this expression, it is straightforward to break down the losses in a solar cell into five factors representing different physical loss mechanisms, requiring different optimization strategies. These key factors are summed up

in Table 2. The corresponding ratios of different losses in our control and optimized devices are exhibited in Figure 4A. Note that these ratios are plotted on a logarithmic axis. A higher percentage (59.55%) of the DB limit efficiency is achieved for both-modified devices, whereas the PCE of control devices reaches only 40.664% and the bottom-modification device reaches 54.219%.

The photocurrent loss $J_{SC}/J_{SC}^{\text{DB}}$ (orange, Figure 4A) is similar for both the bottom and both devices while higher than the control device. From Figure 3B, the film deposited on NiO_x shows a lower quantum efficiency, while deposited on NiO_x/PEAI can improve the quantum efficiency and increase the device's current density. In addition, the bottom-modified film still shows insufficient quantum efficiency in the short-wavelength range, while the both-PEAI-modified film can further increase quantum efficiency (Figure S7). The FF of a solar cell is governed by recombination and resistance.³³ Thus, the FF loss FF/FF^{DB} depends on two parts: the nonradiative loss $\text{FF}_0(V_{OC})/\text{FF}^{\text{DB}}$ (blue, Figure 4A) that is due to the V_{OC} loss relative to the DB model and the loss $\text{F}_{\text{FF}}^{\text{res}} = \text{FF} - \text{FF}_0(V_{OC})$ (pink, Figure 4A) that is due to resistive effects (series and shunt resistance).²⁹ Here, the FF_0 is given by the empirical equation:

$$\text{FF}_0 = \frac{\frac{qV_{OC}}{n_{id}K_B T} - \ln\left(\frac{qV_{OC}}{n_{id}K_B T} + 0.72\right)}{\frac{qV_{OC}}{n_{id}K_B T} + 1} \quad (2)$$

where K_B is the Boltzmann constant, T the device temperature, and n_{id} is the ideality factor. Consistent with the high V_{OC} of 1.192 V, lower nonradiative FF losses were achieved for the optimized PSCs. Additionally, their resistive losses ($\text{F}_{\text{FF}}^{\text{res}}$) decreased compared to those of control devices. This trend is evident in Figure 4B, where the loss $\Delta\text{FF}_2 = \text{FF}_0(V_{OC}) - \text{FF}$ decreases from 22.78% to 8.25% for both-modified PSCs. Overall, reduced nonradiative and resistive losses contribute to the optimized devices exhibiting a higher FF value. The losses from the V_{OC} deficit can be divided into radiative losses $V_{OC}^{\text{rad}}/V_{OC}^{\text{DB}}$ (yellow, Figure 4A) and nonradiative losses $V_{OC}/V_{OC}^{\text{rad}}$ (green, Figure 4A), as shown in Figure 4A. According to a previous report,³⁰ we calculated the radiative limit V_{OC}^{rad} by combining EQE (Q_e^{EQE}), Q_e^{FTPS} from Fourier transform photocurrent

TABLE 2 The parameter values of the figures of merit for control device and optimized device.

Device	PCE/(PCE ^{DB}) [%]	$J_{SC}/J_{SC}^{\text{DB}}$ [%]	$V_{OC}^{\text{rad}}/V_{OC}^{\text{DB}}$ [%]	$V_{OC}/V_{OC}^{\text{rad}}$ [%]	$\text{FF}_0(V_{OC})/\text{FF}^{\text{DB}}$ [%]	FF/ $\text{FF}_0(V_{OC})$ [%]
Control	40.66	51.86	65.90	76.54	89.63	100.00
Bottom	54.22	62.89	73.10	81.34	91.09	100.00
Both	59.55	67.14	76.01	83.26	91.89	100.00

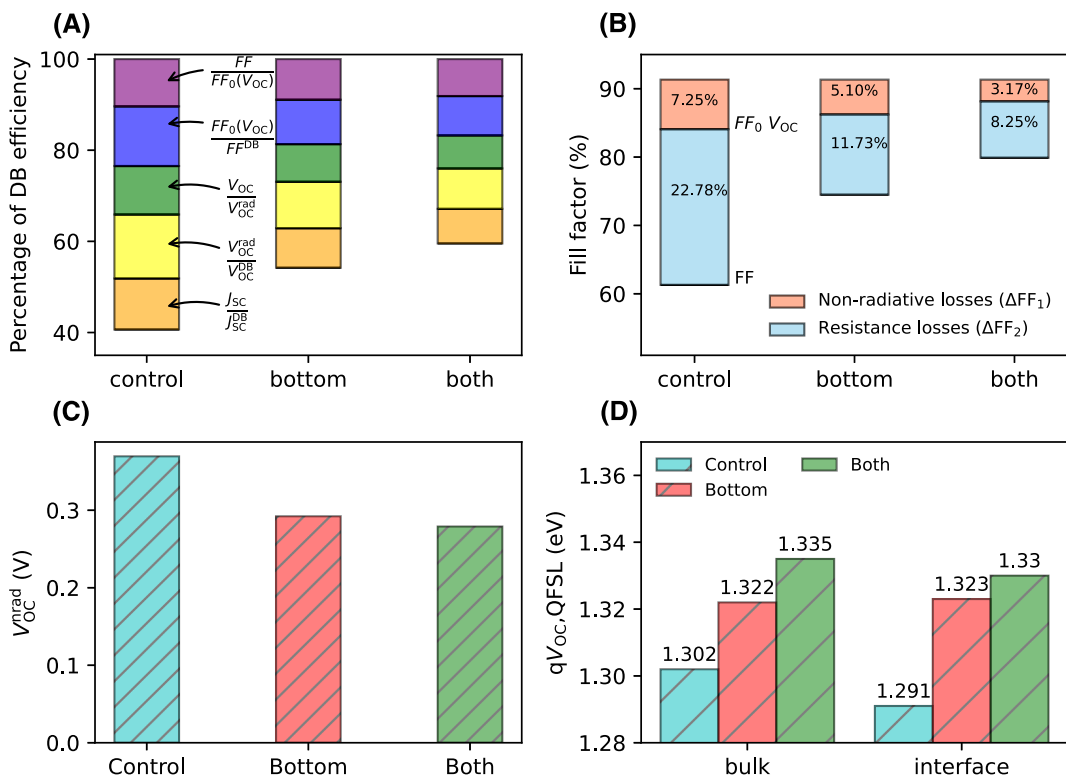


FIGURE 4 (A) Visualization of potential improvement for our devices relative to the ideal DB model, using partitioning of the different losses as introduced in a previous report.²⁹ (B) The detailed fill factor losses of control and optimized devices. (C) V_{OC}^{rad} of the device with or without PEAi modification. (D) QFLS test to uncover the nonradiative occurrences in bulk (glass/(PEAI)/PVK/(PEAI)) and interface (ITO/NiO_x/(PEAI)/PVK/(PEAI)/C₆₀).

spectroscopy, and Q_e^{EL} from electroluminescence (EL) spectra. As shown in Figure S10, the calculated V_{OC}^{rad} values for our control and optimized devices are 1.464, 1.465, and 1.471 V, respectively. Regarding nonradiative recombination losses, $V_{OC}^{\text{nrad}} = V_{OC}^{\text{rad}} - V_{OC}$ for optimized devices is significantly reduced from 0.370 to 0.279 V (Figure 4C). The internal quasi-Fermi level splitting (QFLS) analysis has proven to be an efficient approach for quantifying the origin of energy losses (recombination losses) in perovskites. Here, we use QFLS to differentiate between nonradiative bulk and interface losses. As shown in Figure 4D, both modified devices show higher bulk QFLS and interface QFLS. This result demonstrates that the PEAi can not only reduce bulk nonradiative losses by improving the perovskite film's quality but also reduce interface nonradiative losses via enhanced interface links. Finally, time-resolved photoluminescence (TRPL) was also used to demonstrate carrier extraction in the device. As shown in Figure S11, compared to the control device, the target device exhibits a lower carrier lifetime, which shows that the introduction of PEAi is beneficial to carrier transport in the device.

Then, we fabricated the perovskite/perovskite tandem solar cell to prove the potential of the PEAi on tandem solar cells further. As shown in Figure 5A, the structure

of ITO/NiO_x/(PEAI)/WBG perovskite/(PEAI)/C₆₀/ALD SnO₂/IZO/PEDOT:PSS/NBG perovskite/C₆₀/BCP/Ag was designed in this work. The typical $J-V$ curves of the best-performing tandem solar cells with PEAi modification are shown in Figure 5B. After using PEAi, we can get a high PCE of 26.81% with a J_{SC} of 17.98 mA cm⁻², a V_{OC} of 1.79 V, and an FF of 0.833, and Figure 5C shows the IPCE result of the device with PEAi modification, among them, the integrated current of wide-bandgap PSC is 18.15 mA cm⁻², while the integrated current of narrow-bandgap PSC is 18.01 mA cm⁻², which is consistent with the J_{SC} of all perovskite tandem solar cell. Figure 5D and Figure S12 presents the statistical results of the tandem solar cells with or without PEAi modification. As we can see that the dual-modified tandem devices show a high average PCE compared with the control devices. Figure S13 shows the steady-state output of the all perovskite tandem solar. It can be seen that after 1000 s of continuous operation, the power output of the device is still stable, which means that the device has good working stability. Finally, the stability of the tandem solar cells was tested in a glovebox filled with N₂. As shown in Figure S14, the dual-modified tandem solar cells maintained 86.5% of its initial PCE (26.8%) after aging for 1000 h.

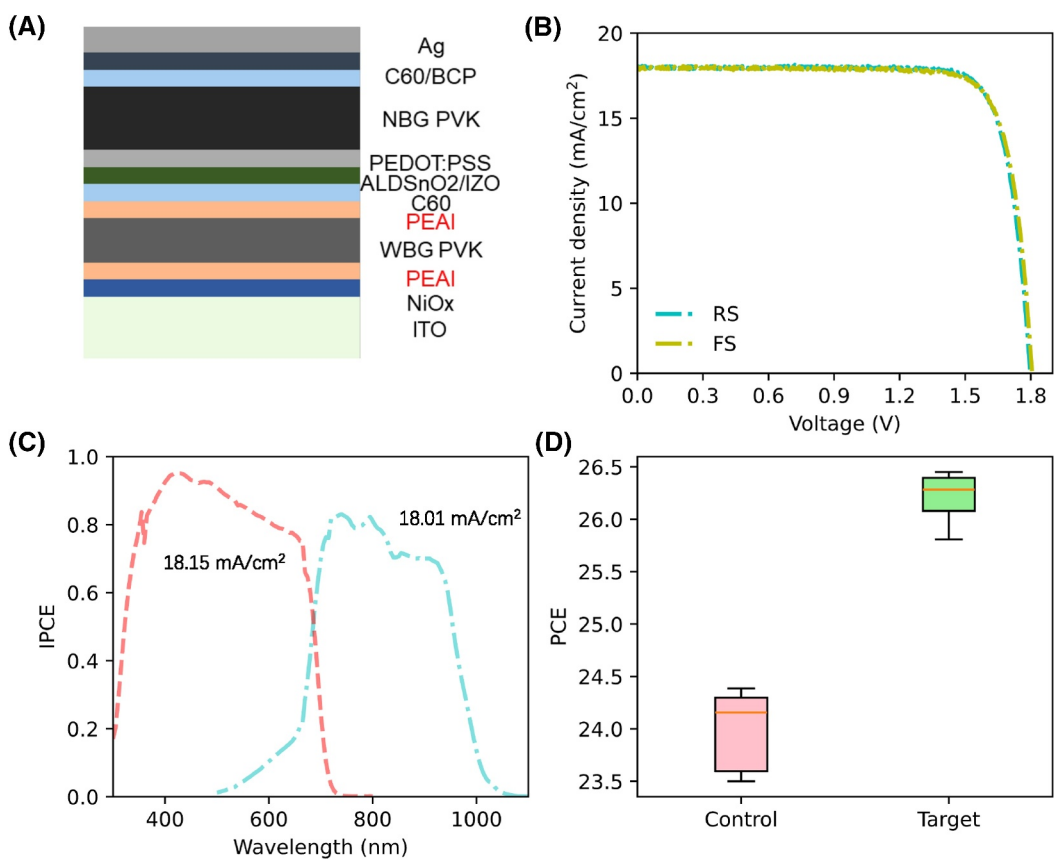


FIGURE 5 (A) Schematic illustration of the tandem solar cell structure in this work. (B) J-V curves and (C) IPCE curves of the device with PEAI co-modification. (D) PCE statistics of the tandem PSCs with or without PEAI co-modification (15 cells were counted).

3 | CONCLUSION

In conclusion, this study introduces a comprehensive passivation approach termed co-interface collaborative passivation. The incorporation of PEAI enhances the perovskite film's quality by diminishing bulk non-radiative recombination and bolstering the film's interfacial adhesion through potent chemical interactions, which in turn mitigates surface defects and further curtails interfacial nonradiative recombination. DFT results corroborate these experimental findings. Ultimately, devices employing this co-modification strategy exhibited an efficiency of 16.5% in single-junction PSCs and 26.81% in all-perovskite tandem solar cells. This research not only offers a blueprint for the development of co-modification strategies but also promotes the further commercialization of PSCs.

4 | EXPERIMENTAL DETAILS

4.1 | Materials

All chemical reagents were used as received without further purification. Xi'an Polymer Light Technology

Corp. supplied PTAA. PCBM, FAI, CsI, PbBr₂, and PbI₂ were purchased from Advanced Electron Technology CO., Ltd. PEAI, FABr, MAI, and MABr were obtained from Tokyo Chemical Industry Co., Ltd. Sigma Aldrich provided EDA, CsBr, SnI₂, SnF₂, GuASCN, BCP, and C₆₀. All solvents were purchased from Sigma Aldrich. PEDOT:PSS aqueous solution (Al 4083) was purchased from Heraeus Clevios. NiO_x was synthesized based on previous reports.³⁴

4.2 | Device fabrication

ITO glasses were ultrasonically cleaned for 20 min in sequence with detergent water and isopropyl alcohol. Then the ITO was treated for 5 min with plasma. Then the glasses were transformed into the glove box. 20 mg NiO_x was dissolved in 1 mL water and stirred for 10 min at room temperature. Then the NiO_x was spin-coated on the ITO with the speed of 4000 rpm for the 30 s, followed by annealing at 100°C for 10 min. For bottom PEAI modification: 1 mg of PEAI was dissolved in 1 mL IPA and this solution was spinning coated on the NiO_x at a speed of 5000 rpm for the 30 s. Then the substrate was put on the hot stage at a temperature of 100°C for 10 min.

The perovskite precursor solution was prepared by dissolving FAI (99.05 mg), CsI (37.41 mg), FABr (47.98 mg), PbI₂ (331.93 mg), PbBr₂ (176.16 mg), and CsBr (20.43 mg) in 1 mL of DMSO/DMF (1/4, v/v) mixture. The perovskite film was deposited using the two-step spin-coating method at 2000 rpm for 10 s and 6000 rpm for the 40 s, with 150 μ L of CB antisolvent dripped over perovskite films for 30 s before the program was terminated, and the film was subsequently annealed at 100°C for 10 min. For top PEAI modification: 1 mg/mL PEAI was dissolved in IPA, and then was spin-coated on the perovskite film at a speed of 5000 rpm for the 30 s. Then the substrate was put on the hot stage at a temperature of 100°C for 10 min. After cooling to room temperature, the substrates were transferred to the evaporation system. Finally, C₆₀ (20 nm), BCP (7 nm), and Ag (100 nm) were sequentially deposited on top of the perovskite by thermal evaporation under a vacuum of 5×10^{-5} Pa through using a shadow mask.

The Tandem PSC was prepared in the following way (here, the concentration of the wide bandgap perovskite precursor solution is increased to 1.3 M). After depositing the C₆₀ on the wide bandgap perovskite film, the substrates were then transferred to the ALD system to deposit 20 nm SnO₂ at 100°C. Tetrakis-(dimethylamino) tin (iv) and deionized water were employed as the precursor. After ALD-SnO₂ deposition, the substrates were transferred to the magnetron sputtering system to deposit 100 nm IZO on the ALD-SnO₂. The PEDOT:PSS layer was spin-cast on IZO and annealed at 120°C for 20 min. Then the narrow bandgap perovskite was prepared on the PEDOT: PSS. We adopted our previous preparation technology³⁵: NBG-PVK solution was obtained by mixing Cs_{0.05}FA_{0.95}SnI₃ (1.8 M), MAPbI₃ (1.8 M) (with 13.23 mg of GuASCN as additive) and MAPbBr₃ (1.8 M) in a certain volume ratio. The perovskite precursor was then dropped onto the PEDOT:PSS and spin-coated at 1000 rpm for 10 s, followed by 5000 rpm for 50 s. 750 μ L toluene was dropped at 20 s from the beginning, followed by heating at 100°C for 5 min. The perovskite layer was then passivated by EDA (0.1 mM in toluene) molecules by employing a spin coater. Next, PCBM (7.5 mg/mL in CB) was coated at 5000 rpm for 50 s, followed by heating at 75°C for 5 min. Finally, C₆₀(20 nm), BCP (7 nm), and Ag (100 nm) were deposited under high vacuum conditions by thermal evaporation to give the tandem PSC.

4.3 | Characterization

X-ray photoelectron spectroscopy (XPS, JPS-9200 spectrometer, JEOL) was used to analyze the surface chemistry state. A Mg target was used for generating the

1253.6 eV light as an X-ray source. Spectra were collected with a step of 0.1 and 10 eV pass energy. The absorbance spectra were collected by using UV-vis spectroscopy (V-670 Spectrophotometer, JASCO), with a background of air. The PLQY of the perovskite film was obtained with an integrating sphere of an Absolute PL Quantum Yield Spectrometer system (C11347, Hamamatsu Photonics, Hamamatsu, Japan). Photoluminescence (PL) spectroscopy and TRPL Spectroscopy (Quantaurus Tau, Hamamatsu) were collected with an excitation laser of 465 nm. XRD patterns were obtained by using an X-ray diffractometer (SmartLab/R/K α 1/RE, Rigaku). The characterization of solar cell devices was executed by using a system source meter (Model 2611A, Keithley) under a solar simulator (CEP-2000SRR, Bunkoukeiki). The light source was calibrated by using two kinds of standard solar cells (BS-520BK and BS-500IR76, Bunkoukeiki) for the xenon lamp and halogen lamp. For measurements under illumination, the mask size of 0.1 and 0.04 cm² were used. The integrated J_{SC} from EQE data is based on the ASTM G173-03 Reference Spectra (Global tilt). Calculations were performed within the Density Functional (DFT) formalism using the Perdew-Burke-Ernzerhof (PBE) GGA exchange-correlation functional.³⁶ All calculations were performed utilizing the CP2K package within Gaussian-augmented plane waves dual basis set using the molecularly optimized MOLOPT double ξ -valence polarized basis set implemented in CP2K code which has a very small Basis Set Superposition Errors in gas and condensed phases.^{37,38} The grid cutoff was 450 Ry. The structural minimization was performed with the help of the Broyden-Fletcher-Goldfarb-Shanno algorithm (BFGS). Multiwfn 3.8 (dev) is used to analyze the calculation results.³⁹

ACKNOWLEDGMENTS

This work was supported by the NEDO project, the New Energy and Industrial Technology Development (JPNP20015).

CONFLICT OF INTEREST STATEMENT

The authors declare no competing financial interest.

DATA AVAILABILITY STATEMENT

The data that support the findings of this study are available in the supplementary material of this article.

ORCID

Huan Bi  <https://orcid.org/0000-0001-7680-9816>

Jiaqi Liu  <https://orcid.org/0000-0002-5738-4741>

Liang Wang  <https://orcid.org/0000-0002-6381-1148>

Zheng Zhang  <https://orcid.org/0000-0002-1568-2732>

Gaurav Kapil  <https://orcid.org/0000-0002-5066-4978>

- Shahrir Razey Sahamir*  <https://orcid.org/0000-0002-9167-5980>
- Ajay Kumar Baranwal*  <https://orcid.org/0000-0003-4582-4532>
- Yuyao Wei*  <https://orcid.org/0000-0002-6449-2169>
- Takeshi Kitamura*  <https://orcid.org/0009-0005-2782-4549>
- Hiroshi Segawa*  <https://orcid.org/0000-0001-8076-9722>
- Qing Shen*  <https://orcid.org/0000-0001-8359-3275>
- Shuzi Hayase*  <https://orcid.org/0000-0002-0756-4808>

REFERENCES

- Zhao R, Wang P, Wang L, et al. *Adv Funct Mater.* 2023; 2307559.
- Cho S, Pandey P, Yoon S, et al. Anchoring self-assembled monolayer at perovskite/hole collector interface for wide bandgap Sn-based solar cells with a record efficiency over 12%. *Surface Interfaces.* 2023;42:103478.
- NREL. Best Research-Cell Efficiency Chart. Accessed September 30, 2023. <https://www.nrel.gov/pv/cell-efficiency.html>
- Bi H, Liu J, Zhang Z, et al. All-perovskite tandem solar cells approach 26.5% efficiency by employing wide bandgap lead perovskite solar cells with New monomolecular hole transport layer. *ACS Energy Lett.* 2023;8(9):3852-3859.
- He R, Ren S, Chen C, et al. Wide-bandgap organic-inorganic hybrid and all-inorganic perovskite solar cells and their application in all-perovskite tandem solar cells. *Energy Environ Sci.* 2021;14(11):5723-5759.
- Wang C, Song Z, Li C, Zhao D, Yan Y. Low-bandgap mixed tin-lead perovskites and their applications in all-perovskite tandem solar cells. *Adv Funct Mater.* 2019;29(47):1808801.
- Hu S, Otsuka K, Murdey R, et al. Optimized carrier extraction at interfaces for 23.6% efficient tin-lead perovskite solar cells. *Energy Environ Sci.* 2022;15(5):2096-2107.
- Yin X, Guo Y, Xie H, Que W, Kong LB. Nickel oxide as efficient hole transport materials for perovskite solar cells. *Sol RRL.* 2019;3(5):1900001.
- Li C, Zhang Y, Zhang X, et al. Engineered oxygen factories synergize with STING agonist to remodel tumor microenvironment for cancer immunotherapy. *Adv Funct Mater.* 2023; 33(41):2214774.
- Ma F, Zhao Y, Li J, Zhang X, Gu H, You J. Nickel oxide for inverted structure perovskite solar cells. *J Energy Chem.* 2021; 52:393-411.
- Chen W, Zhou Y, Wang L, et al. Molecule-Doped nickel oxide: verified charge transfer and planar inverted mixed cation perovskite solar cell. *Adv Mater.* 2018;30(20):1800515.
- Dai J, Xiong J, Liu N, et al. Synergistic dual-interface modification strategy for highly reproducible and efficient PTAA-based inverted perovskite solar cells. *Chem Eng J.* 2023;453: 139988.
- Feng M, Wang Y, Liu F, et al. *Sol RRL.* 2023;2300712.
- Xu L, Chen X, Jin J, et al. Inverted perovskite solar cells employing doped NiO hole transport layers: a review. *Nano Energy.* 2019;63:103860.
- Stolterfoht M, Caprioglio P, Wolff CM, et al. The impact of energy alignment and interfacial recombination on the internal and external open-circuit voltage of perovskite solar cells. *Energy Environ Sci.* 2019;12(9):2778-2788.
- Ye F, Zhang S, Warby J, et al. Overcoming C₆₀-induced interfacial recombination in inverted perovskite solar cells by electron-transporting carborane. *Nat Commun.* 2022;13(1): 7454.
- Liu T, Scheidt RA, Zheng X, et al. Tuning interfacial energetics with surface ligands to enhance perovskite solar cell performance. *Cell Rep Phys Sci.* 2023;4(11):101650.
- Liu W, Xiong J, Liu N, et al. Defect passivation and interface modification by tetra-n-octadecyl ammonium bromide for efficient and stable inverted perovskite solar cells. *Chem Eng J.* 2022;429:132426.
- Bi H, Guo Y, Guo M, et al. Reduced interfacial recombination losses and lead leakage in lead-based perovskite solar cells using 2D/3D perovskite engineering. *J Power Sources.* 2023; 563:232825.
- Bi H, Han G, Guo M, et al. Top-contacts-interface engineering for high-performance perovskite solar cell with reducing lead leakage. *Sol RRL.* 2022;6(9):2200352.
- Zhang F, Ye S, Zhang H, et al. Comprehensive passivation strategy for achieving inverted perovskite solar cells with efficiency exceeding 23% by trap passivation and ion constraint. *Nano Energy.* 2021;89:106370.
- Lab 3: fourier transform infrared spectroscopy (FTIR), Accessed May 11, 2023. <https://chem.libretexts.org/>
- Ren N, Sun C, Zhu C, et al. Triple hole transporting and passivation layers for efficient NiO_x-based wide-bandgap perovskite solar cells. *Appl Phys Lett.* 2023;122(22):223903.
- Bi H, Liu B, He D, et al. Interfacial defect passivation and stress release by multifunctional KPF₆ modification for planar perovskite solar cells with enhanced efficiency and stability. *Chem Eng J.* 2021;418:129375.
- Ding C, Wang D, Liu D, et al. Over 15% efficiency PbS quantum-dot solar cells by synergistic effects of three interface engineering: reducing nonradiative recombination and balancing charge carrier extraction. *Adv Energy Mater.* 2022;12(35): 2201676.
- Caddeo C, Marongiu D, Meloni S, et al. Hydrophilicity and water contact angle on methylammonium lead iodide. *Adv Mater Interfaces.* 2018;6(3):1801173.
- Cojocaru L, Uchida S, Sanehira Y, Nakazaki J, Kubo T, Segawa H. Surface treatment of the compact TiO₂ layer for efficient planar heterojunction perovskite solar cells. *Chem Lett.* 2015; 44(5):674-676.
- Dunfield SP, Bliss L, Zhang F, et al. From defects to degradation: a mechanistic understanding of degradation in perovskite solar cell devices and modules. *Adv Energy Mater.* 2020; 10(26):1904054.
- Guillemoles J-F, Kirchartz T, Cahen D, Rau U. Guide for the perplexed to the Shockley-Queisser model for solar cells. *Nat Photonics.* 2019;13(8):501-505.
- Krückemeier L, Rau U, Stolterfoht M, Kirchartz T. How to report record open-circuit voltages in lead-halide perovskite solar cells. *Adv Energy Mater.* 2019;10(1):1902573.
- Chuang C-HM. Shockley-Queisser-limit. 2016. <https://github.com/marcus-cmc/Shockley-Queisser-limit>
- contributors W. Shockley-Queisser limit; 2024. https://en.wikipedia.org/wiki/Shockley-Queisser_limit

33. Tian J, Zhang K, Xie Z, et al. Quantifying the energy losses in CsPbI₂Br perovskite solar cells with an open-circuit voltage of up to 1.45 V. *ACS Energy Lett.* 2022;7(11):4071-4080.
34. Han Q, Wei Y, Lin R, et al. Low-temperature processed inorganic hole transport layer for efficient and stable mixed Pb-Sn low-bandgap perovskite solar cells. *Sci Bull.* 2019;64(19):1399-1401.
35. Kapil G, Bessho T, Sanehira Y, et al. Tin-lead perovskite solar cells fabricated on hole selective monolayers. *ACS Energy Lett.* 2022;7(3):966-974.
36. Perdew JP, Burke K, Ernzerhof M. Generalized gradient approximation made simple. *Phys Rev Lett.* 1996;77(18):3865-3868.
37. Kühne TD, Iannuzzi M, Del Ben M, et al. CP2K: an electronic structure and molecular dynamics software package - quick-step: Efficient and accurate electronic structure calculations. *J Chem Phys.* 2020;152(19):194103.
38. Takaluoma TT, Laasonen K, Laitinen RS. Molecular dynamics simulation of the solid-state topochemical polymerization of S₂N₂. *Inorg Chem.* 2013;52(8):4648-4657.
39. Lu T, Chen F. Multiwfn: a multifunctional wavefunction analyzer. *J Comput Chem.* 2012;33(5):580-592.

SUPPORTING INFORMATION

Additional supporting information can be found online in the Supporting Information section at the end of this article.

How to cite this article: Bi H, Liu J, Wang L, et al. Double side passivation of phenylethyl ammonium iodide for all perovskite tandem solar cell with efficiency of 26.8%. *EcoEnergy*. 2024;2(3):369-380. <https://doi.org/10.1002/ece2.51>